



Available online at [www.sciencedirect.com](http://www.sciencedirect.com)



ScienceDirect

Trans. Nonferrous Met. Soc. China 28(2018) 998–1006

Transactions of  
Nonferrous Metals  
Society of China

[www.tnmsc.cn](http://www.tnmsc.cn)



## Effect of clad ratio on interfacial microstructure and properties of cladding billets via direct-chill casting process

Hai-tao ZHANG, Xing HAN, Dong-tao WANG, Bo SHAO, Ke QIN, Jian-zhong CUI

Key Laboratory of Electromagnetic Processing of Materials, Ministry of Education,  
Northeastern University, Shenyang 110819, China

Received 8 November 2016; accepted 16 May 2017

**Abstract:** Numerical simulation and experiments were introduced to develop AA4045/AA3003 cladding billets with different clad-ratios. The temperature fields, microstructures and mechanical properties near interface were investigated in detail. The results show that cladding billets with different clad-ratios were fabricated successfully. Si and Mn elements diffused across the bonding interface and formed diffusion layer. With the increase of clad-layer thickness, the interfacial region transforms from semisolid–solid state to liquid–solid state and the diffusion layer increased from 10 to 25  $\mu\text{m}$ . The hardness at interface is higher than that of AA3003 side but lower than that of the other side. The bonding strength increased with the clad-layer thickness, attributing to solution strengthening due to elements diffusion. The cladding billets were extruded into clad pipe by indirect extrusion process after homogenization. The clad pipe remained the interfacial characteristics of as-cast cladding billet and the heredity of clad-ratio during deformation was testified.

**Key words:** cladding billet; clad ratio; temperature field; interfacial microstructure; diffusion layer; bonding strength

### 1 Introduction

Cladding materials, which combine two or more alloys, have attracted increasing attention due to their unique corrosion resistance, specific strength, surface property, and so on [1]. Lots of fabricating processes for it, such as rolling [2], drawing and extrusion [3], solid state diffusion [4], have been studied successfully. In recent years, casting, as a novel process to prepare cladding materials, has garnered significant attention because it is more efficient and economical than other processes. BENEDYK [5] developed Novelis Fusion Process<sup>TM</sup> that broke breakthrough in the simultaneous DC casting of multiple aluminum alloy layers for rolling ingot. ETIENNE et al [6] and MASSIMO et al [7] conducted the study of AA3003/AA4045 clad ingots using a laboratory-scale Fusion<sup>TM</sup> Technology co-casting apparatus, obtained the relationship between the quality of the metallurgical bonding and the predicted thermal history at the interface and investigated the interface formation process in Fusion<sup>TM</sup> casting. FU et al [8]

investigated Al–1Mn and Al–10Si alloy circular clad ingot prepared by semi-continuous casting. However, there are few reports of the effect of clad ratio on interfacial temperature, microstructure and mechanical property, which is necessary to be taken into consideration for the construction of cladding materials.

The clad ratio, which means the percentage of thickness of clad layer from the total, plays a significant role in the subsequent brazing process [9]. During brazing process, when the clad ratio is too low, the brazing filler metal would be in short supply, resulting in the rosin joint or tack weld which is against the heat conductivity and ruggedness of the heat exchanger. However, an oversize clad ratio means that the core layer has a relatively small thickness. It is likely to collapse in the brazing process.

In this work, based on our preliminary work [10], AA4045/AA3003 cladding billets in sizes of  $d122\text{ mm}/d110\text{ mm}$  (clad ratio, 9.8%),  $d130\text{ mm}/d110\text{ mm}$  (clad ratio, 15.4%),  $d140\text{ mm}/d110\text{ mm}$  (clad ratio, 21.4%) were prepared by direct-chill casting process. The interfacial temperature field, microstructure, mechanical

**Foundation item:** Project (2015B090926013) supported by the Science and Technology Program of Guangdong Province, China; Project (20170540307) supported by the Natural Science Foundation of Liaoning Province, China

**Corresponding author:** Hai-tao ZHANG; Tel: +86-24-83681431; Fax: +86-24-83681758; E-mail: [haitao\\_zhang@epm.neu.edu.cn](mailto:haitao_zhang@epm.neu.edu.cn)  
DOI: 10.1016/S1003-6326(18)64736-3

property and indirect extrusion were comprehensively investigated. This work was focused on the interface formation process with different clad ratios and determination of the relationship between the interfacial characteristics and the clad ratio.

## 2 Experimental

As commonly used commercial alloys, AA4045 has high strength and good weldability, and AA3003 is a wrought Al–Mn alloy which has excellent corrosion resistance and moderate strength. The combination of them could combine their advantages and be applied to condenser pipe, radiators and heat exchangers [11]. The chemical compositions are listed in Table 1.

**Table 1** Alloy compositions used in present work (mass fraction, %)

Alloy	Si	Fe	Cu	Mn	Mg	Zn	Ti	Al
AA3003	0.6	0.7	0.05– 0.20	1.0– 1.5	–	0.10	–	Bal.
AA4045	9.0– 11.0	0.8	0.30	0.05	0.05	0.10	0.20	Bal.

The apparatus of direct-chill casting for fabricating cladding billets was designed and shown in Fig. 1. When the temperatures of AA3003 and AA4045 reached 720 and 740 °C, respectively, the former was poured into the inner-crystallizer firstly and held for several seconds to form supporting layer under the cooling of the inner-mold. Then, the latter was poured into the outer-crystallizer rapidly and flowed into the outer-crystallizer. At the same time, the starting head began to work. Subsequently, the two alloys contacted and bonded. Finally, the cladding billets were prepared successfully.

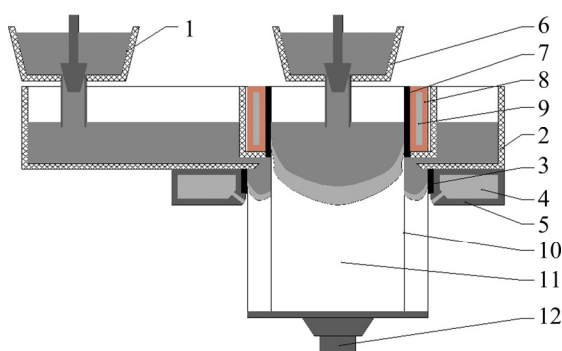


**Fig. 1** Schematic diagram of cladding casting equipment: 1—Clad tundish; 2—Launder; 3—Outer-graphite; 4—Cooling water; 5—Outer-mold; 6—Core tundish; 7—Inner-graphite; 8—Inner-mold; 9—Cooling water; 10—Bonding interface; 11—Cladding billet; 12—Starting head

In order to investigate interfacial characteristics of the cladding billets, the cross section, after lathed, was corroded to observe macrostructure by an ambient solution of 10% (mass fraction) NaOH in 10 min, and sample for metalloscope and scanning electron microscope (SEM, Zeiss Ultra Plus 60) was etched by a solution of 5% (volume fraction) HF in 15 s. The Vickers hardness was measured with a test load of 3 N and a dwell time of 15 s. Using a MTS-810 universal testing machine, shear tests were performed qualitatively by a home-made set-up, as shown in Fig. 2. The cladding billet was indirectly extruded into clad pipe.

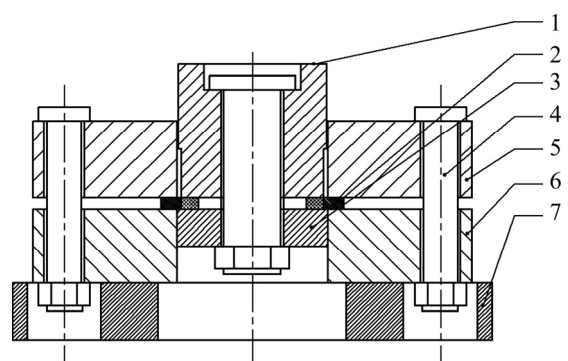


**Fig. 2** Schematic diagram of home-made die for testing shear strength of cladding bar: 1—Punch; 2—Sample; 3—Gland; 4—Fastening bolt; 5—Upper die; 6—Lower die; 7—Pedestal

## 3 Simulation model and numerical procedure

### 3.1 Assumptions and simplified mathematic model

1) In this model, the calculation of the solute field is not included.

2) The molten aluminum alloys behave as an incompressible fluid, so the density of the melt is the constant. But the thermal buoyancy must be included in this model, therefore the Boussinesq approximation is used to calculate the thermal buoyancy and is expressed as

$$F_{\text{thermal}} = \rho g \beta (T - T_0) \quad (1)$$

where  $\rho$  and  $\beta$  are the density and the volume expansion coefficient of the molten aluminum, respectively.  $T_0$  is the reference temperature and is frequently given as the temperature when the dendrite coherence occurs.

3) In the process of AA4045/AA3003 cladding billet, the solidified part moves along the axial with casting speed.

### 3.2 Governing equations

In this work, based on governing equations applied to all regions (liquid, mushy and solid zone) of solidification system, a single domain volume-average

model is used. All these regions are implicitly defined within the system by distributions of energy determined from the solutions model equations, which are expressed as follows:

Conservation equation of mass:

$$\nabla \cdot U = 0 \quad (2)$$

Conservation equation of momentum:

$$\nabla \cdot (\rho U U) = \nabla \cdot (\mu_{\text{eff}} \nabla U) - \nabla P + S_m \quad (3)$$

where  $\mu_{\text{eff}}$  and  $S_m$  are effective viscosity and momentum source, respectively. The effective viscosity  $\mu_{\text{eff}}$  is given by  $\mu_{\text{eff}} = \mu_l + \mu_t$ , where  $\mu_l$  is laminar viscosity in the liquid and  $\mu_t$  is turbulent viscosity. The momentum source  $S_m$  includes thermal buoyancy and Darcy source term.

Conservation equation of energy:

$$\nabla \cdot (\rho U T) = \nabla \cdot \left( \frac{k}{c_p} \nabla T \right) + S_{\text{th}} \quad (4)$$

where  $S_{\text{th}}$  is thermal source, i.e., latent heat of solidification.

In this model, the standard  $\kappa-\varepsilon$  model, which is a semiempirical model, is used to model transport of turbulence kinetic energy ( $k$ ) and its dissipation rate ( $\varepsilon$ ). The first form of this model was proposed by Harlow and Nagayama and suggested that

$$\mu_t = \rho C_\mu \frac{k^2}{\varepsilon} \quad (5)$$

where  $C_\mu$  is a function of the turbulent Reynolds number which is a constant value;  $k$  and  $\varepsilon$  are the turbulence kinetic energy and its rate of dissipation, respectively, and obtained from the following transport equations:

$$\nabla \cdot (\rho U k) = \nabla \left( \mu_l + \frac{\mu_t}{\sigma_k} \right) + G_k - \rho \varepsilon - \frac{\mu_l}{K+x} k \quad (6)$$

$$\begin{aligned} \nabla \cdot (\rho U \varepsilon) = & \nabla \left[ \left( \mu_l + \frac{\mu_t}{\sigma_\varepsilon} \right) \nabla \varepsilon \right] + \\ & C_1 \frac{\varepsilon}{k} G_k - C_2 \rho \frac{\varepsilon^2}{k} - \frac{\mu_l}{K+x} \varepsilon \end{aligned} \quad (7)$$

where  $k$  and  $x$  are permeability and very small positive number to avoid diverging of conversation equations. Permeability  $k$  is given as a function of solid fraction  $f_s$ , i.e.,  $k = k_0 (1 - f_s)^3 / f_s^2$ .  $G_k$  represents the generation of turbulence kinetic energy due to the mean velocity gradients, calculated as follows:  $G_k = -\rho \mu' \mu_j' (\partial \mu_j / \partial x_i)$ .  $C_1$  and  $C_2$  are constants.  $\sigma_k$  and  $\sigma_\varepsilon$  are the turbulent Prandtl number for  $\kappa$  and  $\varepsilon$ , respectively. All constants, which are used in the model, are listed in Table 2.

### 3.3 Physical properties

The thermophysical properties and other material

properties of the alloys used during the calculation procedure are listed in Table 3. The thermal properties of the alloys were calculated by JMat-Pro, and the results of specific heat, thermal conductivity and fraction solid are shown in Fig. 3, Fig. 4 and Fig. 5, respectively.

**Table 2** Constant used in  $\kappa-\varepsilon$  model

$C_1$	$C_2$	$\sigma_k$	$\sigma_\varepsilon$	$C_\mu$
1.44	1.92	1.0	1.3	0.09

**Table 3** Physical properties and constant used in numerical simulation

Physical property	AA3003	AA4045
Density, $\rho$ /(kg·m <sup>-3</sup> )	2520	2420
Liquidus temperature, $T_l$ /K	931	868
Solidus temperature, $T_s$ /K	918	850
Latent heat of fusion, $L$ /(J·kg <sup>-1</sup> )	$3.9 \times 10^5$	$4.7 \times 10^5$
Volume expansion coefficient, $\beta$ /K <sup>-1</sup>	$6.7 \times 10^{-5}$	$5.2 \times 10^{-5}$
Distribution coefficient of solute, $k_0$	0.16	0.70
Initial permeability, $K_0$	$2 \times 10^{-11}$	$2 \times 10^{-11}$
Solid fraction of dendrite contact, $f^*$	0.3	0.25

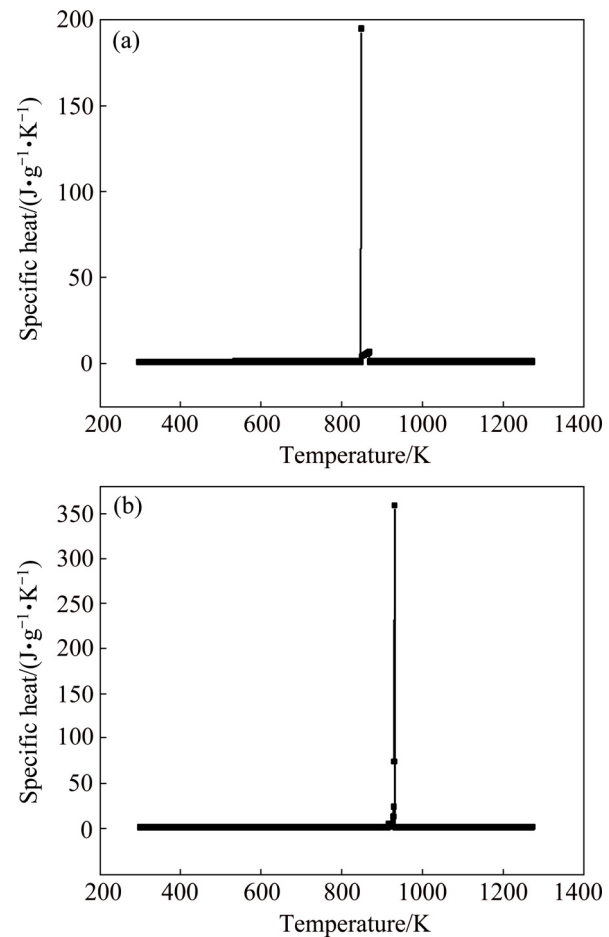


**Fig. 3** Specific heat of aluminum alloys: (a) AA3003; (b) AA4045

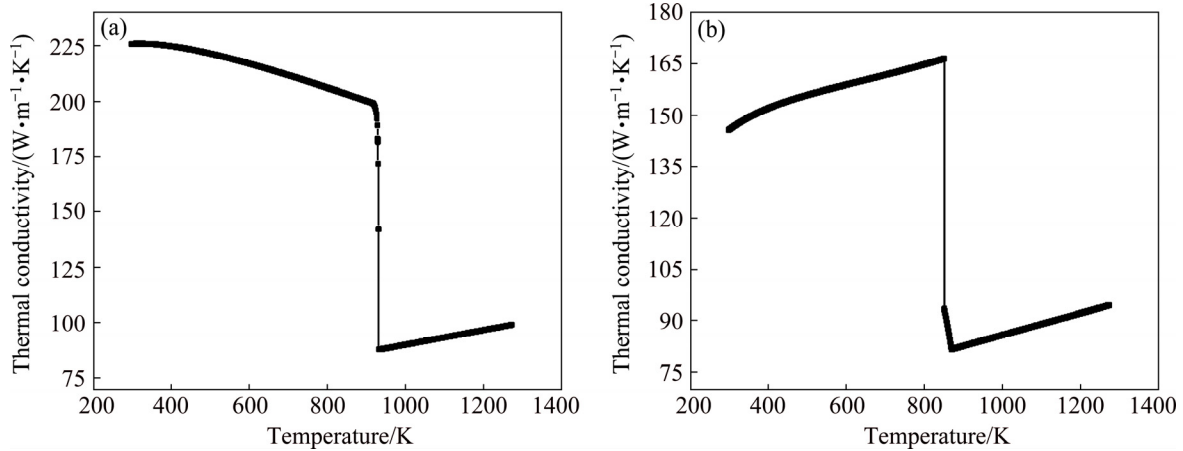


Fig. 4 Thermal conductivity of aluminum alloys: (a) AA3003; (b) AA4045

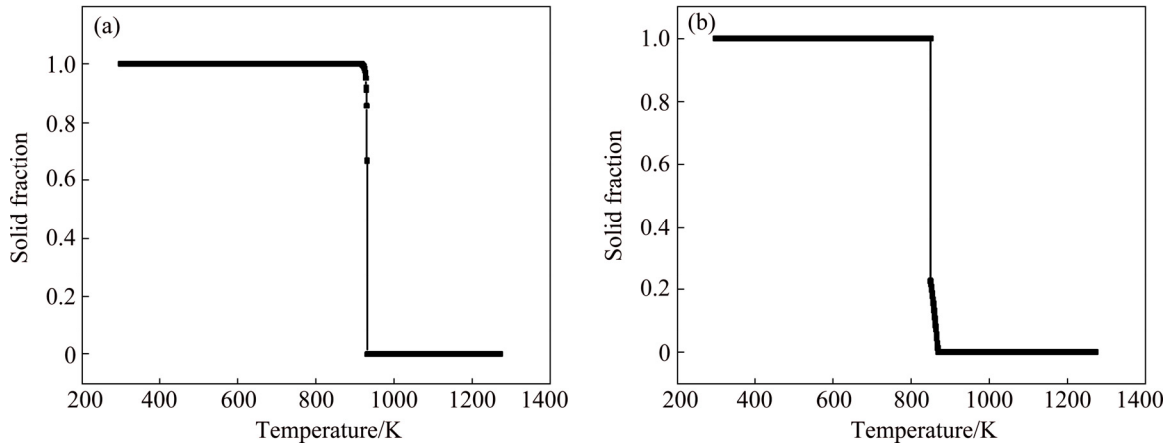


Fig. 5 Solid fraction of aluminum alloys: (a) AA3003; (b) AA4045

### 3.4 Boundary conditions

Based on Ref. [12], boundary conditions applied on the computational domain (as shown in Fig. 6) are described as follows:

1) Inlets and outlets: All the boundary conditions in the region are constant values and listed in Table 4 and  $R_{noz}$  is the hydraulic radius of inlet.

2) Free surface: The thermal boundary conditions are treated as Cauchy-type boundary condition and expressed in Eq. (8), and the heat transfer coefficient  $h$  is constant, 50 W/(m<sup>2</sup>·K).

$$\lambda \frac{\partial T}{\partial n} = h(T - T_{en}) \quad (8)$$

where  $T_{en}$  is environment temperature, 300 K.

3) Primary cooling: The velocity and turbulence boundary conditions are set to the static wall; the thermal boundary condition is treated as Cauchy-type boundary condition, which is formulate according to Eq. (8), and the heat transfer coefficient between the mold and the melt is assumed to vary with the solid fraction and is written according to

$$h = h_{\text{contact}} (1 - f_s) + h_{\text{air}} \times f_s \quad (9)$$

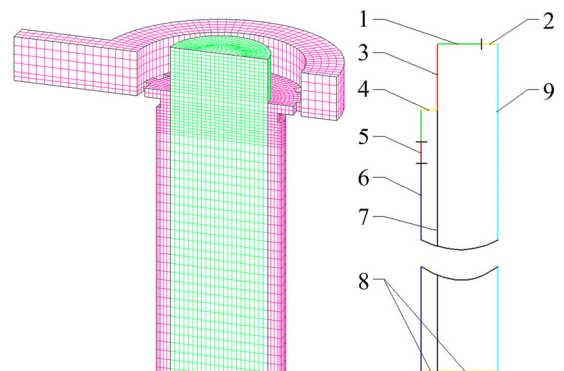


Fig. 6 Mesh model and boundary conditions: 1—Free surface; 2—Inlet-AA3003; 3—Inner mold; 4—Inlet-AA4045; 5—Outer mold; 6—Second cooling; 7—Interface; 8—Outlet; 9—Symmetry axis

where  $h_{\text{contact}}$  reflects good thermal contact between the mold and the melt and is given as 3000 W/(m<sup>2</sup>·K);  $h_{\text{air}}$  is equal to 100 W/(m<sup>2</sup>·K) to reflect poor thermal contact associated with the gap formed when the melt is solidified [12].

4) Secondary cooling: The velocity and turbulence boundary condition are treated as the moving wall and its moving velocity is the casting speed. In terms of the

thermal boundary condition, the secondary cooling boundary is divided into two zones, that is the impingement zone and the streaming zone. They are also Cauchy-type boundary condition and their heat transfer coefficients are shown in Fig. 7. In addition, the environment temperature is given as 300 K.

5) Composite interface: The interface of the two alloys is treated as stationary wall relatively, and the heat transfer of them is coupled.

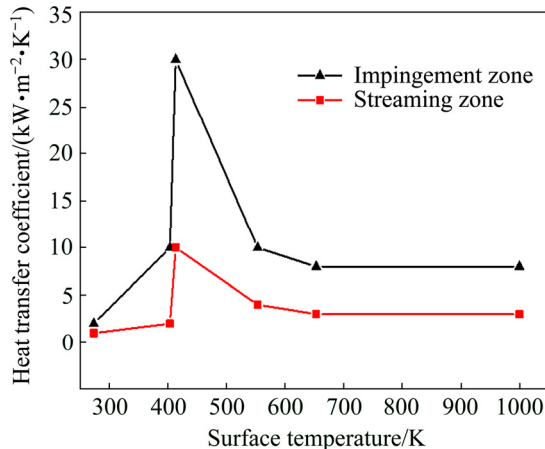


Fig. 7 Variation of heat transfer coefficient with wall surface temperature at secondary cooling zone

6) Symmetry axis: This boundary is set to axisymmetric boundary condition.

## 4 Results and discussion

### 4.1 Temperature field in interfacial region

In order to make the two alloys bond metallurgically, the temperature distribution and variation in the interfacial region play significant roles. The interfacial region is in liquid-solid state when AA4045 contacts with the supporting layer of AA3003, then transforms into semisolid-solid state, and turns into solid-solid state finally. Elements diffusion mainly occurs in the first state, i.e., effective diffusion, but can be ignored in the last state relatively. In addition, the temperature when AA4045 contacts with the supporting layer of AA3003 is defined as contact temperature.

The calculated results of temperature field of cladding with different clad ratios are shown in Fig. 8. It can be seen that clad ratio has a great influence on the interfacial temperature field, while little impact on the solidification of AA3003.

Particularly, the temperature field of interfacial region is magnified and tagged with two-phase regions of two alloys, as shown in Fig. 9. Under the cooling of

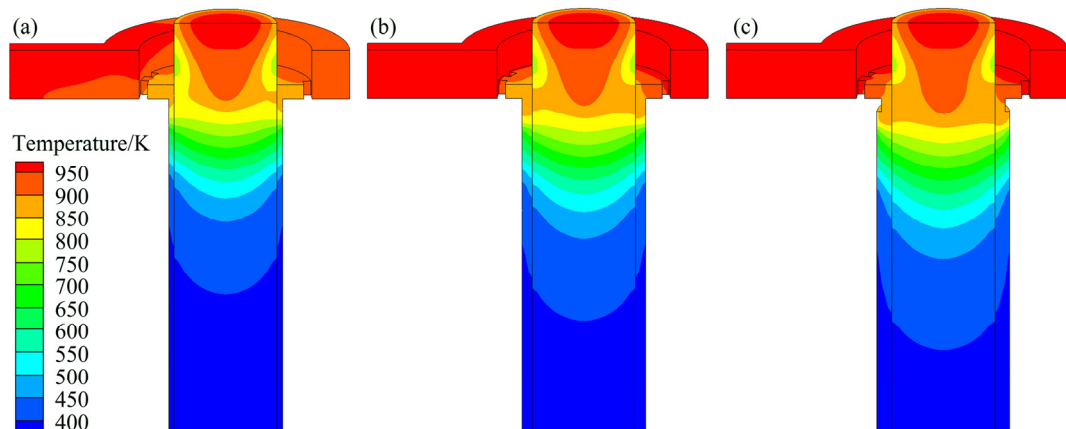


Fig. 8 3D surface plots of temperature field with different clad-layer thicknesses: (a) 6 mm; (b) 10 mm; (c) 15 mm

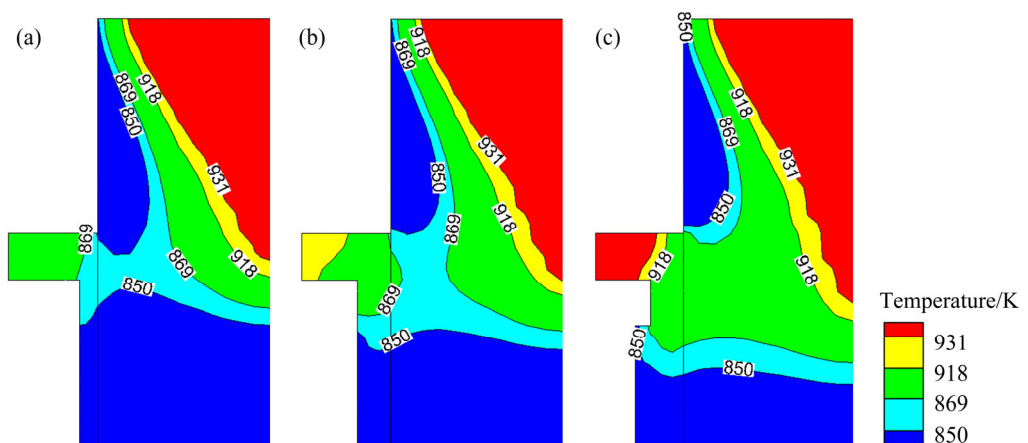


Fig. 9 2D surface plots of two-phase regions with different clad-layer thicknesses: (a) 6 mm; (b) 10 mm; (c) 15 mm

inner-mold, AA3003 melt starts to solidify and forms solid supporting layer, and the supporting layer is observably reheated by AA4045 melt. With the increase of clad-layer thickness, the interfacial region transforms from semisolid–solid state to liquid–solid state, promoting predictably elements diffusion. In addition, the change of temperature gradient in the interfacial region cannot be neglected. Temperature gradient affects solidification direction and rate, thus affecting microstructure and diffusion layer.

#### 4.2 Microstructures and mechanical properties of as-cast cladding billets

The macrostructures and microstructures are displayed in Fig. 10. The two alloy layers are revealed by two different contrasts. The interfaces separate the two layers clearly, as shown in Figs. 10(a), (b) and (c). In AA4045 side, the microstructure is characterized by the dendritic  $\alpha$ (Al) and acicular eutectic silicon crystals and some phases containing manganese are embedded in the  $\alpha$ (Al) matrix in AA3003 part. There are no discontinuities, cracks or porosities in the interface region, indicating a well bonding of the two alloys.

Distinct difference of interfacial microstructure exists among the cladding billets with different clad ratios. As shown in Fig. 9(a) and Fig. 10(d), when the contact temperature was lower than 869 K, AA4045 melt had started to solidify and eutectic Si was precipitated at the interface. Because of reheat phenomenon, some low-temperature phase in the supporting layer was remelted and separated out along the interface due to inverse segregation caused by solidifying

contraction [13], as marked in Fig. 10(a). With the increase of the clad-layer thickness, the contact temperature gradually exceeded 869 K and the liquid–solid state in the interfacial region would be kept for some time, as shown in Figs. 9(b) and (c). Under the influence of outer-mold and second cooling water, primary  $\alpha$ (Al) formed based on the supporting layer, then eutectic Si was precipitated and Mn element diffused sufficiently across the interface and solved into the aluminum substrate, as shown in Figs. 10(e) and (f).

Therefore, it is the original interface temperature and the temperature gradient of the interfacial region that lead to the microstructure difference.

In order to investigate the effect of clad ratio on element diffusion in the interfacial region, the energy dispersive spectrometer (EDS) analysis was introduced, as displayed in Fig. 11. The Si element in AA4045 side and the Mn element in AA3003 side diffused into the other side, and formed a diffusion layer. The thickness of the diffusion layer increased with the clad layer, i.e., 10  $\mu\text{m}$  diffusion layer (6 mm clad layer), 20  $\mu\text{m}$  diffusion layer (10 mm clad layer), and 25  $\mu\text{m}$  diffusion layer (15 mm clad layer).

Figure 12 shows the Vickers hardness in the interfacial region of the as-cast cladding billet. It can be seen that the average values of hardness of AA4045 matrix and AA3003 matrix are about HV 65 and HV 45, respectively. The hardness around the bonding interface is higher than that of AA3003 side but lower than that of the other side because of the interdiffusion of the alloy elements. In addition, the thicker the clad layer is, the higher the hardness of the interface becomes. From

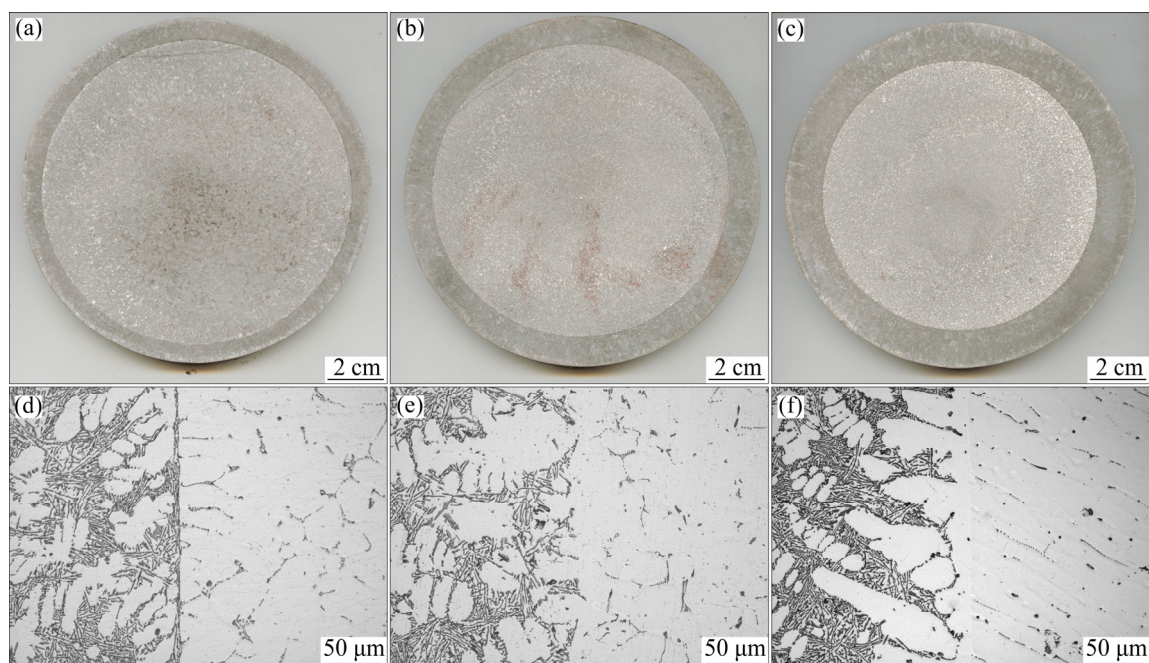


**Fig. 10** Macrostructures (a–c) and interfacial microstructures (d–f) of cladding billets with different clad-layer thicknesses: (a, d) 6 mm; (b, e) 10 mm; (c, f) 15 mm

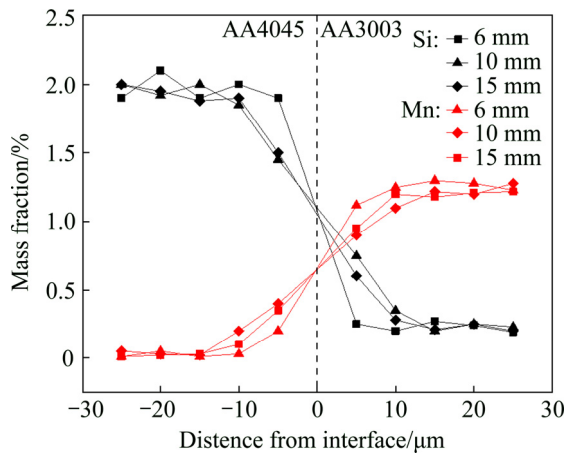


Fig. 11 Distribution of alloying elements near interface with different clad-layer thicknesses

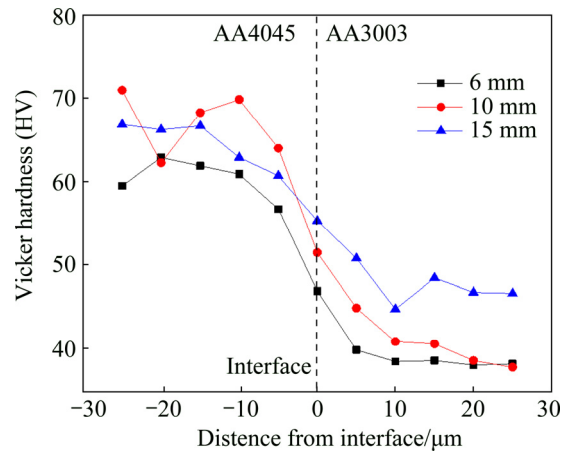


Fig. 12 Vickers hardness profiles across interface with different clad-layer thicknesses

Ref. [14], the Vickers hardness  $H$  and yield strength  $\sigma_y$  of the material approximately obey the three times relationship, i.e.  $H \approx 3\sigma_y$ . Therefore, it can be indicated that the interface yield strength is also higher than that of AA3003.

The shear strength is a directly efficient approach to judge the bonding quality of two alloys and a significant

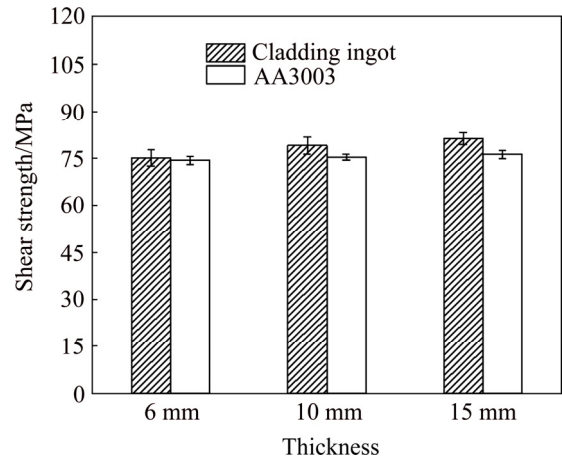


Fig. 13 Shear strength of interface with different clad-layer thicknesses

parameter during plastic deformation. The shear strength is shown in Fig. 13. The shear strength increased with the clad-layer thickness, attributing to solution strengthening due to elements diffusion. With the increase of the clad-layer thickness, the contact temperature obtained an obvious enhance and the liquid-solid state in the interfacial region would be kept for more time, facilitating elements diffusion.

Moreover, all the shear strength was not lower than that of AA3003, indicating that relative slip of two alloys would be avoided during deformation process.

#### 4.3 Extrusion

In order to release the residual stress and eliminate the dendrite segregation of non-equilibrium phases, the cladding billet was homogenized at 560 °C for 12 h, followed by air cooling to room temperature. The temperature of cladding billets rose with heat-up rates of 3 °C/min in the pit-type electric resistance furnace. Then, clad pipe in sizes of  $d32 \text{ mm} \times 2.5 \text{ mm}$  was obtained by the indirect extrusion process. The cross sections of clad pipes were etched by 5% HF for 20 s after polishing, as shown in Fig. 14. It can be seen that the interface is

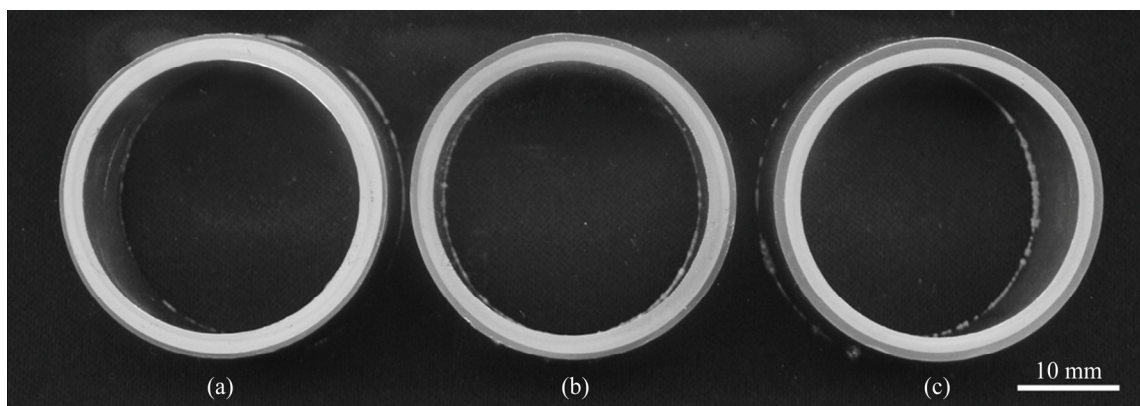
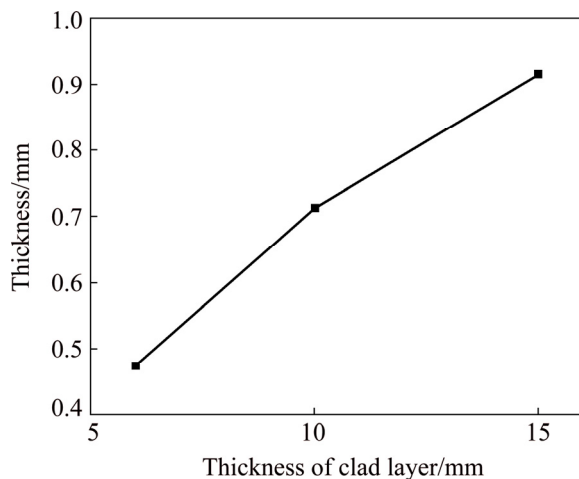


Fig. 14 Photographs of cross sections of clad pipes with different clad-layer thicknesses: (a) 6 mm; (b) 10 mm; (c) 15 mm

characterized by the clear bilaminar feature, which is similar to the as-cast feature. As shown in Fig. 15, the thickness of the clad layer of the clad pipes increases with that of the cladding billets, testifying the heredity of the thickness of clad layer during plastic deformation [15].



**Fig. 15** Thickness of clad layer of clad pipes with different clad-layer thicknesses of cladding billets

## 5 Conclusions

1) Clad ratio has a great influence on the interfacial temperature field. With the increase of clad-layer thickness, the interfacial region transforms from semisolid–solid state to liquid–solid state, promoting predictably elements diffusion.

2) The cladding billets with different clad ratios are fabricated successfully. Si and Mn elements diffused across the bonding interface and formed diffusion layer. The diffusion layer increased from 10 to 25  $\mu\text{m}$  with the clad layer from 6 to 15 mm.

3) The hardness at the interface is higher than that of AA3003 side but lower than that of the other side. The bonding strength increased with the clad-layer thickness, attributing to solution strengthening due to elements diffusion.

4) The cladding billets were extruded into clad pipe by the indirect extrusion process after homogenization. The clad pipe remained the interfacial characteristics of as-cast cladding billet and the heredity of the clad during deformation was testified.

## References

- MILLER W S, ZHUANG L, BOTTEMA J, WITTEBROOD A J, SMET P D, HASZLER A, VIEREGGE A. Recent development in aluminium alloys for the automotive industry [J]. Materials Science and Engineering A, 2000, 280: 37–49.
- QUADIR M Z, FERRY M, AL-BUHAMAD O, MUNROE P R. Shear banding and recrystallization texture development in a multilayered Al alloy sheet produced by accumulative roll bonding [J]. Acta Materialia, 2009, 57(1): 29–40.
- SPONSELLER D L, TIMMONS G A, BAKKER W T. Development of clad boiler tubes extruded from bimetallic centrifugal castings [J]. Journal of Materials Engineering and Performance, 1998, 7(2): 227–238.
- SEQUEIRA C A C, AMARAL L. Role of Kirkendall effect in diffusion processes in solids [J]. Transactions of Nonferrous Metals Society of China, 2014, 24(1): 1–11.
- BENDYK J C. Noveils fusion process: Breakthrough in the simultaneous DC casting of multiple aluminum alloy layers for rolling ingot [J]. Light Metal Age, 2006, 8: 48–50.
- ETIENNE J F R C, ROSE E O P, AMIR R B, MARY A W, DAVID C W, SIMON B, MARK G. Direct-chill co-casting of AA3003/AA4045 aluminum ingots via Fusion™ Technology [J]. Metallurgical and Materials Transactions B, 2014, 45B(3): 975–987.
- MASSIMO D, CARON E J F R, WECKMAN D C, WELLS M A. Interface formation during Fusion™ casting of AA3003/AA4045 aluminum alloy ingots [J]. Metallurgical and Materials Transactions B, 2015, 46(6): 2674–2691.
- FU Ying, JIE Jin-chuan, WU L, PARK J, SUN Jian-bo, KIM J, LI Ting-ju. Microstructure and mechanical properties of Al–1Mn and Al–10Si alloy circular clad ingot prepared by direct chill casting [J]. Materials Science and Engineering A, 2013, 561: 239–244.
- LIU Zheng-chun, GAN Wei-ping, PENG Zhi-hui, WEI Jia-hong. Determination of the clad ratio of the aluminum alloy brazing sheet for automobile heat exchangers [J]. Journal of Central South University of Technology, 1999, 30(4): 401–403.
- HAN Xing, SHAO Bo, ZUO Ke-sheng, JIANG Lin, ZHANG Hai-tao, HE Li-zi, QIN Ke, CUI Jian-zhong. Microstructure and properties at bonding interface of AA4045/AA3003 aluminum alloy cladding billet prepared by semi-continuous casting [J]. Transactions of Nonferrous Metals Society of China, 2016, 26(3): 658–664.
- YOON J S, LEE S H, KIM M S. Fabrication and brazeability of a three-layer 4343/3003/4343 aluminum clad sheet by rolling [J]. Journal of Materials Processing Technology, 2001, 111(1–3): 85–89.
- ZHANG Hai-tao, NAGAUMI H, ZUO Yu-bo, CUI Jian-zhong. Coupled modeling of electromagnetic field, fluid flow, heat transfer and solidification during low frequency electromagnetic casting of 7XXX aluminum alloys, Part 1: Development of a mathematical model and comparison with experimental results [J]. Materials Science and Engineering A, 2007, 448(1): 189–203.
- DIAO Q Z, TSAI H L. Modeling of solute redistribution in the mushy zone during solidification of aluminum-copper alloys [J]. Metallurgical Transactions A, 1993, 24(4): 963–973.
- ZHANG P, LI S X, ZHANG Z F. General relationship between strength and hardness [J]. Materials Science and Engineering A, 2011, 529: 62–73.
- KO D C, LEE S K, KIM B M, JO H H, JO H. Evaluation of copper coating ratio in steel/copper clad wire drawing [J]. Journal of Materials Processing Technology, 2007, 186(1–3): 22–26.

# 包覆率对直接水冷铸造法制备 包覆铸锭界面组织和性能的影响

张海涛, 韩星, 王东涛, 邵博, 秦克, 崔建忠

东北大学 材料电磁过程研究教育部重点实验室, 沈阳 110819

**摘要:** 采用数值模拟和实验相结合的方法研究了不同包覆率的 AA4045/AA3003 铝合金包覆铸锭的制备, 并对界面处的温度场和组织性能进行了详细分析。结果表明, 采用直接水冷铸造法可得到不同包覆率的铸锭, Si 和 Mn 在界面处发生了互扩散并形成扩散层。随着包覆率的增加, 两种合金接触时界面区域由半固态-固态转变为液态-固态, 界面处硬度由 HV 47 增加到 HV 55, 扩散层厚度由 10 增加到 25  $\mu\text{m}$ 。界面处硬度高于 AA3003 合金一侧, 低于 4045 合金一侧, 这是由元素扩散引起固溶强化造成。均匀化退火后, 在包覆铸锭被反向挤压成复合管材的过程中, 界面处保持层状结构不变, 包覆率在变形过程中的遗传性得到证实。

**关键词:** 包覆铸锭; 包覆率; 温度场; 界面组织; 扩散层; 结合强度

(Edited by Bing YANG)